crystals

MDPI

Article

Impact of Disorder on Properties of Vacancies: A Case Study of B2 and A2 Polymorphs of Non-Stoichiometric Fe_2CoAl

Martin Friák [1,*], Jana Pavlů [2] and Mojmír Šob [2,1]

[1] Institute of Physics of Materials, v.v.i., Czech Academy of Sciences, Žižkova 22, CZ-616 00 Brno, Czech Republic
[2] Department of Chemistry, Faculty of Science, Masaryk University, Kotlářská 2, CZ-611 37 Brno, Czech Republic; houserova@chemi.muni.cz (J.P.); mojmir@ipm.cz (M.Š.)
* Correspondence: friak@ipm.cz

Abstract: We have performed an *ab initio* study of vacancy-induced changes in thermodynamic, structural and magnetic properties of single-phase ferromagnetic Fe_2CoAl with a chemically disordered (i) two-sublattice B2 phase or (ii) single-sublattice A2 phase. The two polymorphs of slightly non-stoichiometric Fe_2CoAl ($Fe_{27}Co_{14}Al_{13}$) were modeled by two different 54-atom supercells with atoms distributed according to the special quasi-random structure (SQS) concept. Both the lower-energy B2 phase and a higher-energy A2 phase possess elastic constants that correspond to an auxetic material that is mechanically stable. The properties of vacancies were computed by systematically removing different atoms (one at a time) from the supercells and quite wide ranges of values of vacancy-related characteristics were obtained. The increase in the level of disorder (when changing from the B2 to the A2 phase) results in an increase in the scatter of calculated values. The Fe and Co vacancies have lower vacancy formation energies than the Al ones. The total magnetic moment of the supercell decreases when introducing Fe and Co vacancies but it increases due to Al ones. The latter findings can be partly explained by an increase of the local magnetic moment of Fe atoms when the number of Al atoms in the first neighbor shell of Fe atoms is reduced, such as due to Al vacancies.

Keywords: Fe_2CoAl; disorder; vacancies; magnetism; ab initio; defects; auxetic

check for updates

Citation: Friák, M.; Pavlů, J.; Šob, M. Impact of Disorder on Properties of Vacancies: A Case Study of B2 and A2 Polymorphs of Non-Stoichiometric Fe_2CoAl. *Crystals* **2021**, *11*, 1207. https://doi.org/10.3390/cryst11101207

Academic Editors: Alberto Girlando

Received: 24 September 2021
Accepted: 4 October 2021
Published: 7 October 2021

1. Introduction

Our study is focused on the Fe_2CoAl intermetallic compound belonging to a very large class of ternary X_2YZ materials with Heusler-type crystal lattice [1]. This family of compounds covers numerous combinations of different chemical elements, see, e.g., high-throughput theoretical studies in refs. [2,3]. This compositional variability provides a wide range of properties [4,5], including magnetic ones [6–8], half-metallic properties that are interesting for spintronic applications [9–13], magneto-optical functionalities [14], topological quantum features [15,16] or, e.g., shape-memory behavior [17–19].

The studied Fe_2CoAl can also be categorized as a material based on iron and aluminium. The very promising class of Fe-Al-based materials [20–27] has been studied very intensively including experimental research [28–40] motivated by (i) possible applications of these materials in high-temperature coatings [41–47] and composites [48–52] or (ii) their preparation by newly emerging techniques [53–56]. Theoretical studies of iron-aluminides cover first-principles calculations of single-phase materials [57–71], combined methodological approaches [72–75], or calculations of properties of defects [76–81].

In our current study, we focus on the properties of vacancies in the disordered Fe_2CoAl with the impact of disorder being illustrated by comparing two structural models with different level of disorder. First, we use a structural model that is based on the experimental work of Grover et al. [82] where a single-phase Fe_2CoAl has effectively a chemically disordered B2 lattice with two sublattices: one containing equal amounts of Fe and Co atoms and the second exhibiting equal amounts of Fe and Al.

We further compare vacancy-related characteristics in the B2 phase with those obtained for a single-sublattice more-disordered A2 phase of Fe_2CoAl. We use quantum-mechanical calculations to determine vacancy-induced changes in (i) thermodynamic properties by evaluating the vacancy formation energy, (ii) total magnetic moment, and (iii) structural properties by analyzing the volumetric changes.

2. Methods

When modeling a partially disordered B2 phase (with two compositionally different sublattices) and a single-sublattice disordered A2 phase of Fe_2CoAl, we have utilized two different 54-atom supercells, see Figure 1a,b, respectively. The atoms on the two B2-phase sublattices and one A2-phase sublattice were distributed according to the special quasi-random structure (SQS) concept [83] as generated by the USPEX software [84–86]. The actual stoichiometry of our supercells, $Fe_{27}Co_{14}Al_{13}$ or $Fe_2Co_{1.037}Al_{0.963}$, slightly deviates from the exact Fe_2CoAl stoichiometry as 54 is not divisible by 4. The cube-shaped 54-atom supercells, $3 \times 3 \times 3$ multiples of a 2-atom B2 cell, are convenient for modeling of elasticity of disordered systems. Single-crystal elastic constants were determined using the stress-strain method [87]. It should be mentioned that our computational supercells, that are used as models for partly-disordered B2 and disordered A2 phase of Fe_2CoAl, do not have their anisotropic elastic properties equal along crystallographic directions that would be equivalent in the case of cubic-symmetry systems, such as along the [100], [010] and [001] directions. The computed differences are small (a few percent), nevertheless, we have used a proper mathematical approach [88] to determine the closest cubic-symmetry elastic tensor and its C_{11}, C_{12} and C_{44} components are reported below.

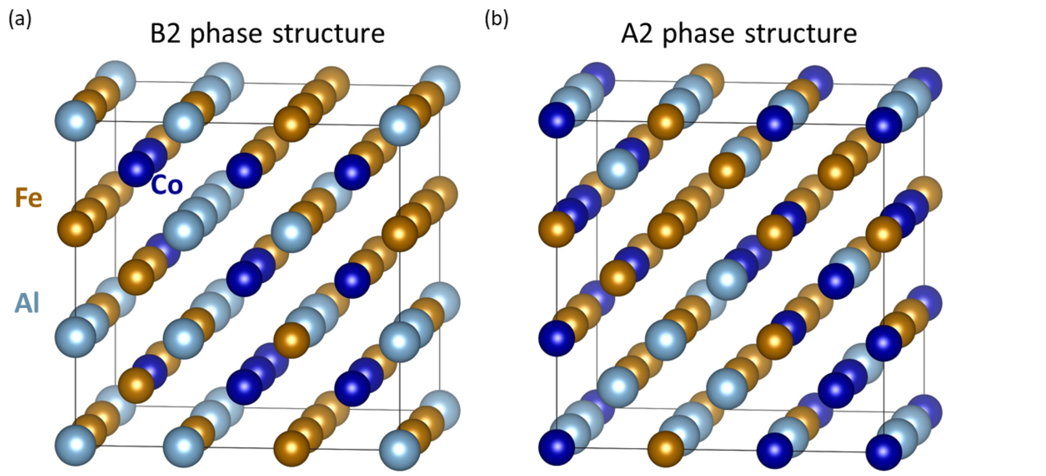

Figure 1. Schematic visualizations of our computational supercells representing the B2 phase (**a**) and A2 phase (**b**) of Fe_2CoAl (some atoms, such as those in the vertices, are shown with their periodic images). The B2 phase exhibits two sublattices–one occupied by an equal amount of Fe and Co, while the other by equal amounts of Fe and Al.

Regarding our quantum-mechanical calculations, we have used the Vienna Ab initio Simulation Package (VASP) [89,90] based on the density functional theory [91,92]. The Projector-Augmented-Wave (PAW) pseudopotentials [93,94] and the Generalized Gradient Approximation (GGA) in the parametrization by Perdew and Wang [95] (PW91) with the Vosko-Wilk-Nusair correction [96] were utilized for the exchange and correlation energy. The plane-wave energy cut-off was equal to 400 eV and a $6 \times 6 \times 6$ Monkhorst-Pack [97] k-point mesh was used in the case of 54-atom supercells in Figure 1 (or their 53-atom variants with a vacancy). We have fully relaxed all studied supercells, i.e., the energy and forces were minimized with respect to atomic positions, cell shape and the volume (forces acting upon atoms were reduced under 0.01 eV/Å). All local magnetic moments were initially set up as parallel.

3. Results

A primary aim of our study consists in properties of vacancies but we will report their characteristics with respect to those of vacancy-free states. Therefore, we start with summarizing thermodynamic, structural and magnetic properties of both the B2 and A2 phases without defects. As the properties of the B2 phase can be found in our previous study [98], we will focus on the A2 phase. First, we analyze the thermodynamic stability by evaluating formation energies. The formation energy E_f per atom is defined as the difference between the energy of the studied phase, in our case, the energy $E(Fe_{27}Co_{14}Al_{13})$ of the 54-atom supercell, and the sum of energies of constituting atoms in their elemental phases, i.e., ferromagnetic (FM) body-centered cubic (bcc) Fe, $E(\text{Fe})$, ferromagnetic hexagonal close-packed (hcp) Co, $E(\text{Co})$, and nonmagnetic (NM) face-centered cubic (fcc) Al, $E(\text{Al})$, weighted by their amount, i.e.,

$$E_f = \left(E(\text{Fe}_{27}\text{Co}_{14}\text{Al}_{13}) - 27 \cdot E(\text{Fe}) - 14 \cdot E(\text{Co}) - 13 \cdot E(\text{Al}) \right) / (27 + 14 + 13).$$

The formation energies of the B2 and A2 phases are equal to −0.243 eV/atom and −0.157 eV/atom, respectively. The disordered A2 phase has a significantly less negative energy and, therefore, a lower thermodynamic stability. It is an excited state with respect to the B2 phase that is supposed to be the ground state as proposed by Grover et al. [82]. The A2 phase has also a higher configurational entropy but the difference is quite small, 0.03 meV/(K·atom), see the Appendix A, and it is only of minor importance. We further check the mechanical stability of the studied phases by determining a set of single-crystal elastic constants (C_{11}, C_{12}, C_{44}) corresponding to a cubic-symmetry system. The A2 phase has them (203 GPa, 140 GPa, 123 GPa) different from those for the more ordered B2 phase (244 GPa, 141 GPa, 131 GPa) [98] but both systems are mechanically stable (fulfill the stability conditions [99]). We visualize the elastic properties of both phases in the form of a directional dependence of Young's modulus in Figure 2 using the MELASA software [100] (open access available online: https://melasa.cerit-sc.cz/ (accessed on 6 October 2021)).

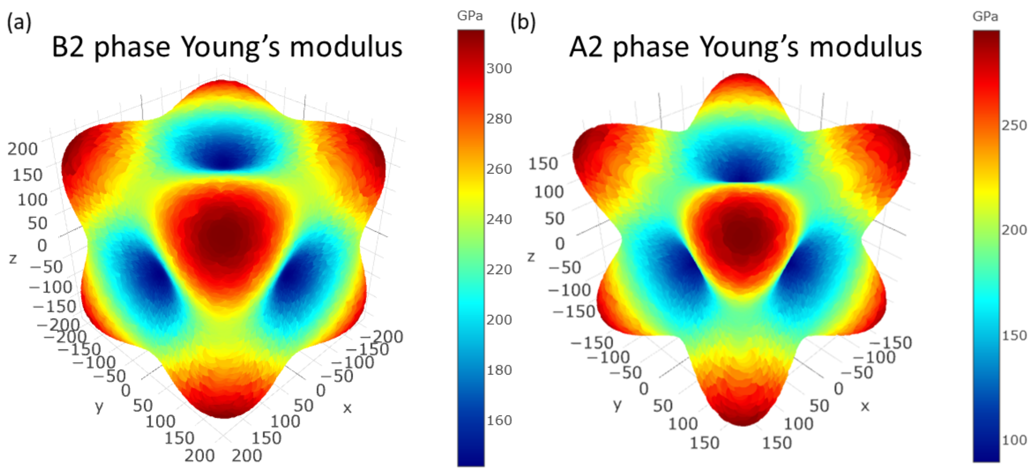

Figure 2. Computed directional dependences of Young's modulus for both the B2 phase (**a**) and A2 phase (**b**) illustrating single-crystal elastic properties. Please mind different ranges of values corresponding to the same color scale.

Further, we have also used the ELATE software [101] (open access at http://progs.coudert.name/elate, accessed on 6 October 2021) to determine both the minimum (−0.243) and the maximum (0.857) value of single-crystal Poisson ratio ν. Interestingly, as our analysis predicts that the Poisson ratio of the A2-phase Fe_2CoAl is negative for certain directions of loading, it is an auxetic material (as was also the case of the B2 phase [98]). Thorough information is provided in Figure 3 that visualizes a directional dependence of both maximum and minimum value of Poisson ratio and the values in the x-z plane (for details, see ref. [101]). The negative values of ν_{min} are marked by red color in Figure 3.

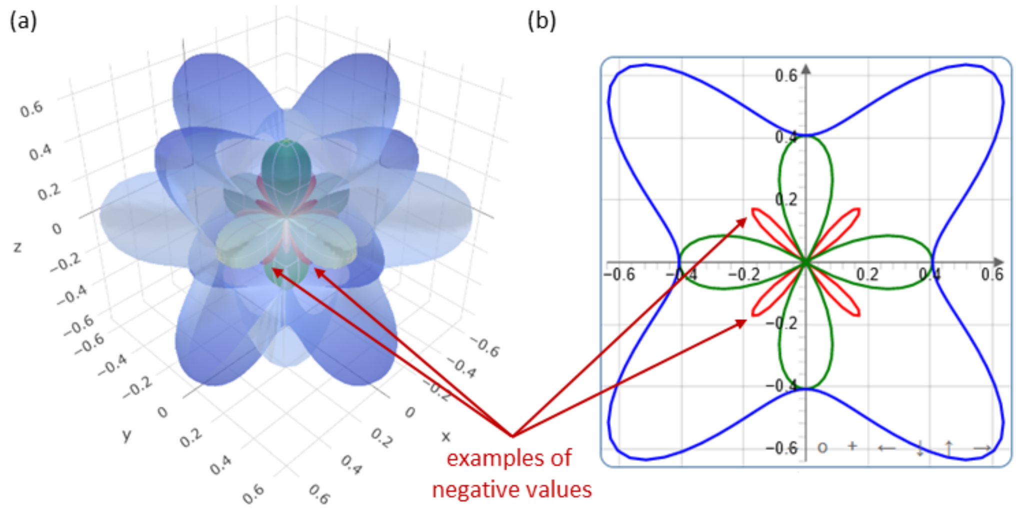

Figure 3. Calculated directional dependence of the minimum and maximum value of Poisson ratio of the A2 phase (**a**) together with a cut in the x-z plane (**b**). The negative values, indicating auxetic properties, are visualized using red color and a few examples are pointed at by red arrows.

Regarding the magnetic properties, the computed local magnetic moments in both the B2 and A2 phase are shown in Figure 4. The total magnetic moment in the case of the B2 phase amounts to 68.26 μ_B per 54-atom supercell, while the A2 phase has the total magnetic moment by 18.7% higher, equal to 81.0 μ_B per 54-atom supercell. Common magneto-volumetric correlations can help us to connect this difference in the total magnetic moment with the fact that the volume of the A2 supercell (641.6 Å^3 per 54-atom supercell) is higher than that of the B2 phase (624.3 Å^3 per 54-atom supercell). Figure 4 also neatly visualizes the differences between the local magnetic moments in the B2 and A2 phases as an illustration of the impact of the different level of order in the B2 and A2 polymorphs.

Next, we systematically remove each of the 54 atoms in each of the two phases to determine the properties of vacancies and compare the results for each atom type.

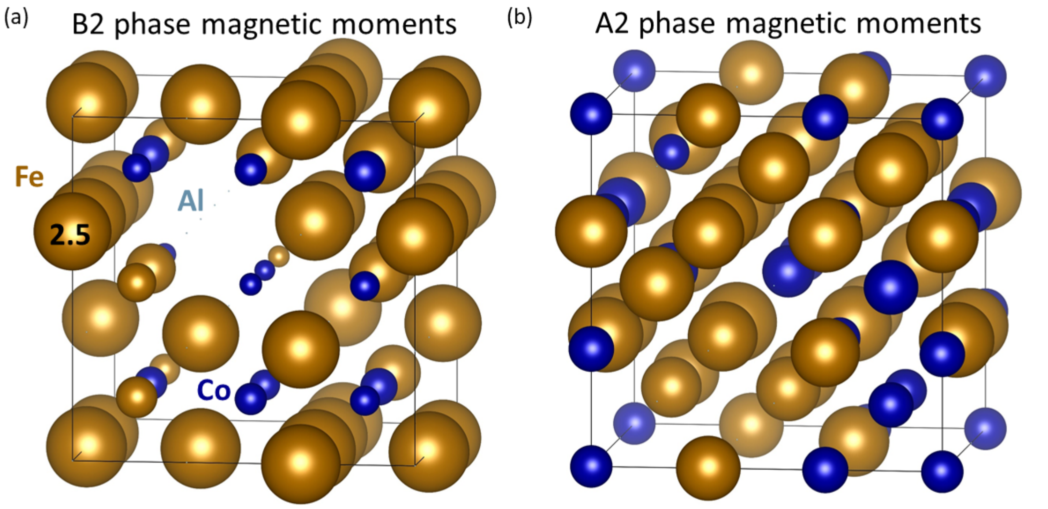

Figure 4. Schematic visualizations of local magnetic moments for the B2 (**a**) and A2 (**b**) phase. The magnitudes of local magnetic moments are indicated by the diameter of the spheres representing the atoms with an example of the scaling shown for one particular Fe atom (2.5 μ_B) in part (**a**).

The computed results in the case of Fe vacancies are shown in Figure 5. The vacancy formation energies ($E(\mathrm{Fe}_{(27-1)}\mathrm{Co}_{14}\mathrm{Al}_{13}$ + $E(\mathrm{Fe})$ $-$ $E(\mathrm{Fe}_{27}\mathrm{Co}_{14}\mathrm{Al}_{13}))$ in Figure 5a,b are quite clearly different for the Fe atoms belonging to the two different sublattices in the B2 phase. The Fe vacancies at the (Fe, Al) sublattice have higher vacancy formation energies, see full circles in Figure 5a, than those at the (Fe, Co) sublattice, full triangles in Figure 5a. The Fe vacancy formation energies in the A2 phase cover a broader range of values, see Figure 5b, including some quite low ones. The difference of the total magnetic moments, $\mu(\mathrm{Fe}_{(27-1)}\mathrm{Co}_{14}\mathrm{Al}_{13}) - \mu(\mathrm{Fe}_{27}\mathrm{Co}_{14}\mathrm{Al}_{13})$, of supercells with and without a vacancy, respectively, is shown in Figure 5c,d. It is mostly negative (the total magnetic moment is lower when a Fe atom is removed). The reduction in the B2 (A2) phase is often smaller (bigger), respectively, than the magnitude of the magnetic moment of FM bcc Fe, 2.2 μ_B, that is indicated by the horizontal dashed line.

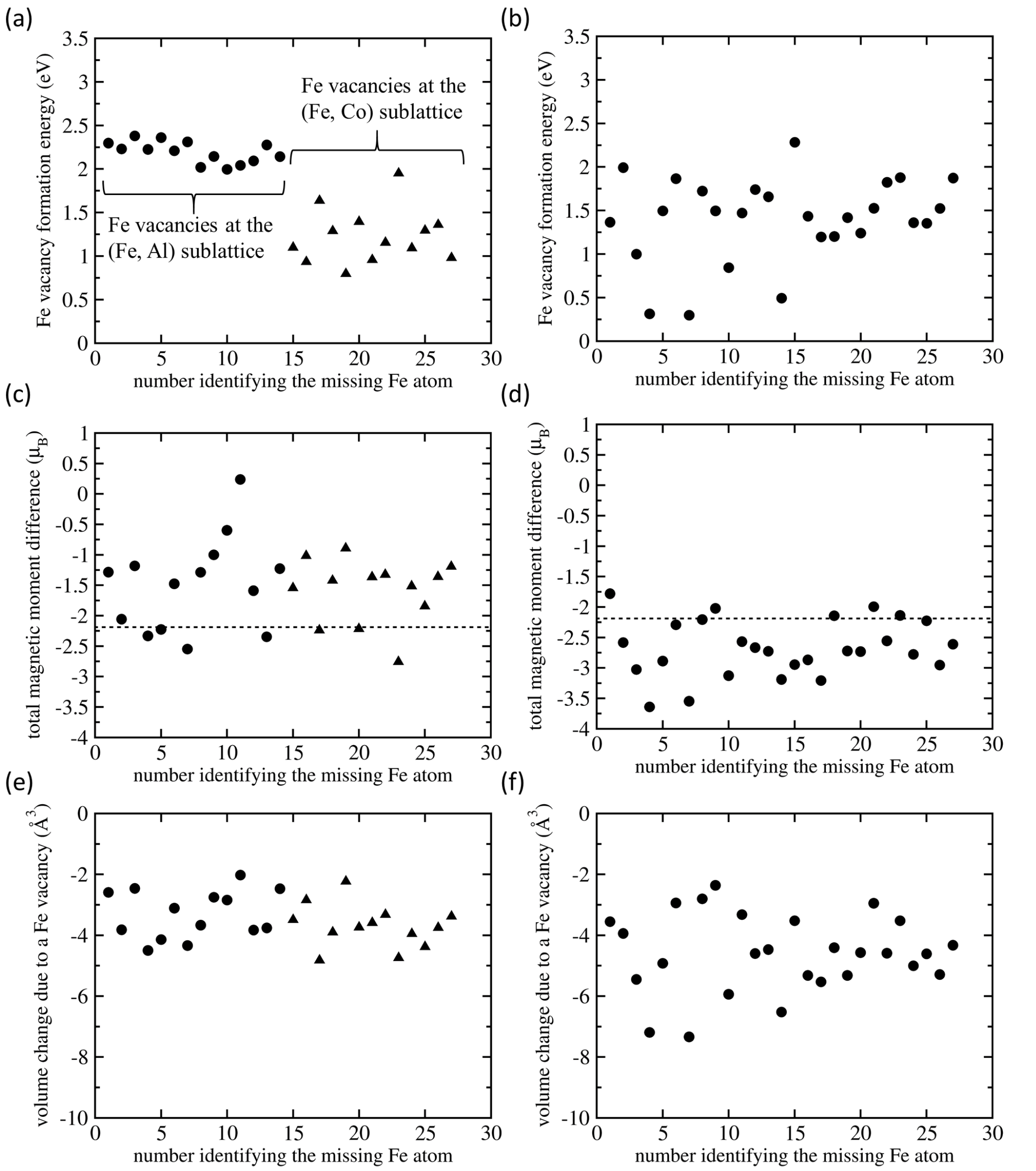

Figure 5. Computed formation energies of Fe vacancies in the B2 (**a**) and A2 (**b**) phase together with the changes of the total magnetic moment of the whole supercell of the B2 (**c**) and A2 (**d**) phase (compared with a hypothetical reduction by the magnetic moment of one FM bcc Fe atom, 2.2 μ_B, see the horizontal dashed line) and the vacancy-induced volumetric change for both the B2 (**e**) and A2 (**f**) phase.

A volume difference $V(\mathrm{Fe}_{(27-1)}\mathrm{Co}_{14}\mathrm{Al}_{13}) - V(\mathrm{Fe}_{27}\mathrm{Co}_{14}\mathrm{Al}_{13})$ of the supercells with and without vacancy, respectively, is negative, see Figure 5e,f, i.e., the volume is reduced due to a missing Fe atom, and the reductions cover a wider range in the A2 phase.

The results for Co vacancies are summarized in Figure 6. There are only 14 Co atoms in the 54-atom supercell representing the B2 and A2 phase and, therefore, the number of data points in Figure 6 is about twice lower than in the case of 27 Fe atoms in Figure 5 discussed above. All the Co atoms are located only in one of the two sublattices in the B2 phase and their vacancy formation energies cover quite a narrow range of values, see Figure 6a. Not having this limitation in the case of the A2 phase, the vacancy formation energies are spread over a wider range, see Figure 6b. Regarding the vacancy-induced change of the total magnetic moment in Figure 6c,d, its value in the B2 (A2) phase is typically reduced by less (more) than the magnitude of the magnetic moment of one FM hcp Co atom, 1.5 μ_B, see the horizontal dashed line in Figure 6c,d.

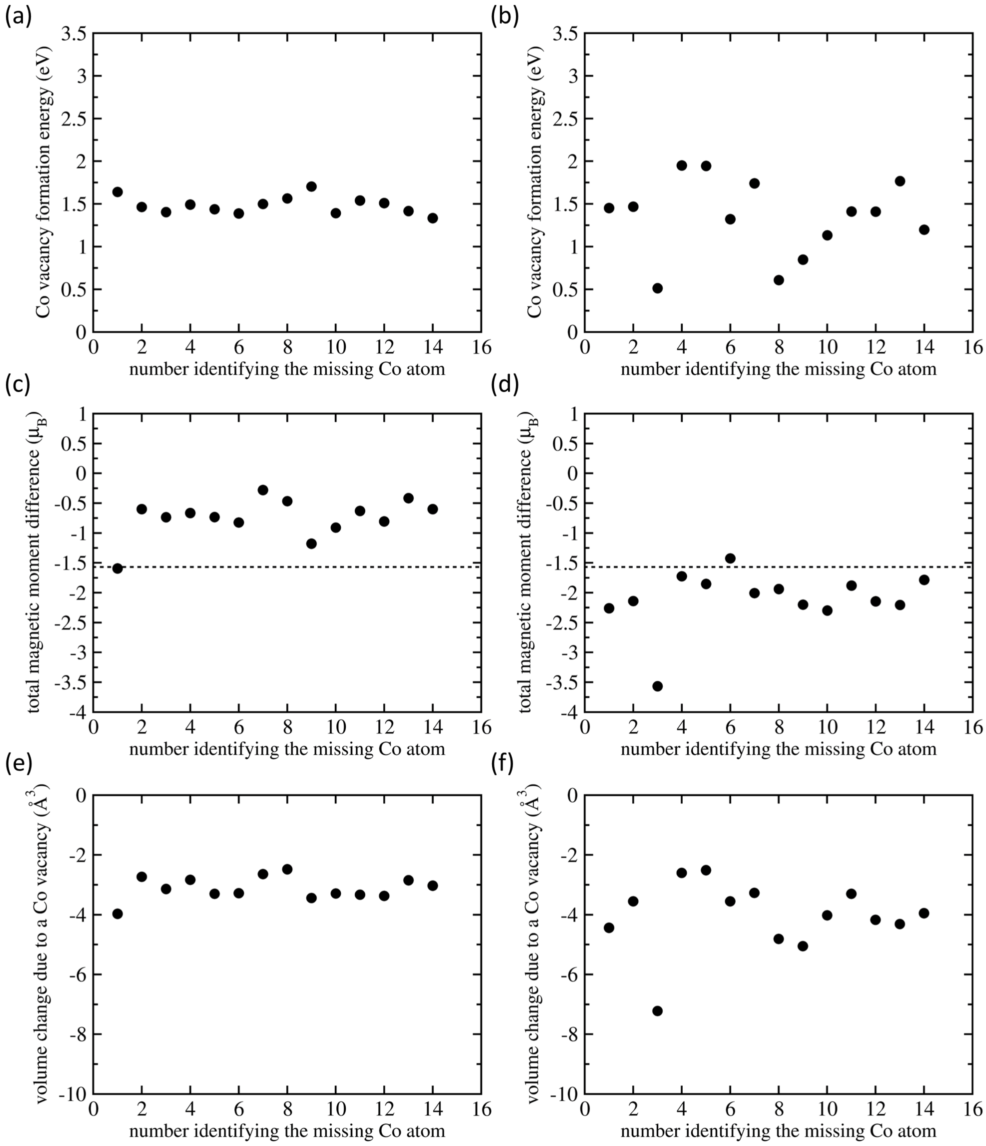

Figure 6. Calculated formation energies of Co vacancies in the B2 (**a**) and A2 (**b**) phase together with the changes of the total magnetic moment of the whole supercell of the B2 (**c**) and A2 (**d**) phase of $\mathrm{Fe_2CoAl}$ (compared with a hypothetical reduction by the magnetic moment of one FM hcp Co atom, 1.5 μ_B, see the horizontal dashed line) and the vacancy-induced volumetric change for both the B2 (**e**) and A2 (**f**) phase.

Our findings related to the volumetric reduction of the supercells due to Co vacancies are very similar to those that we found for Fe vacancies (see above).

Rather different trends are found in the case of Al vacancies, see Figure 7. First, the corresponding Al-vacancy formation energies in Figure 7a are much higher in the B2 phase than those related to Fe and Co vacancies. The change of the ordering from the B2 to the A2 phase leads to a reduction of the vacancy formation energy, cf. Figure 7a,b. Regarding the change of the total magnetic moment due to Al vacancies, it increases very significantly in the B2 phase, see Figure 7c. This increase can be partly explained as an opposite to the reduction of local magnetic moment of Fe atoms when increasing the number of Al atoms in the first nearest neighbor (1NN) shell of Fe atoms. We have reported this trend in Fe-Al alloys [71] or Fe-Al-Ti alloys [102]. As an Al vacancy in the (Fe, Al) sublattice lowers the number of Al atoms in the 1NN shell of Fe atoms in the (Fe, Co) sublattice of the B2 phase, local magnetic moments of Fe atoms from the (Fe, Co) sublattice next to the Al vacancy increase and so does the total magnetic moment of the whole supercell. We previously found an increase of the total magnetic moment due to Al vacancies also in the Fe-Al alloys [77].

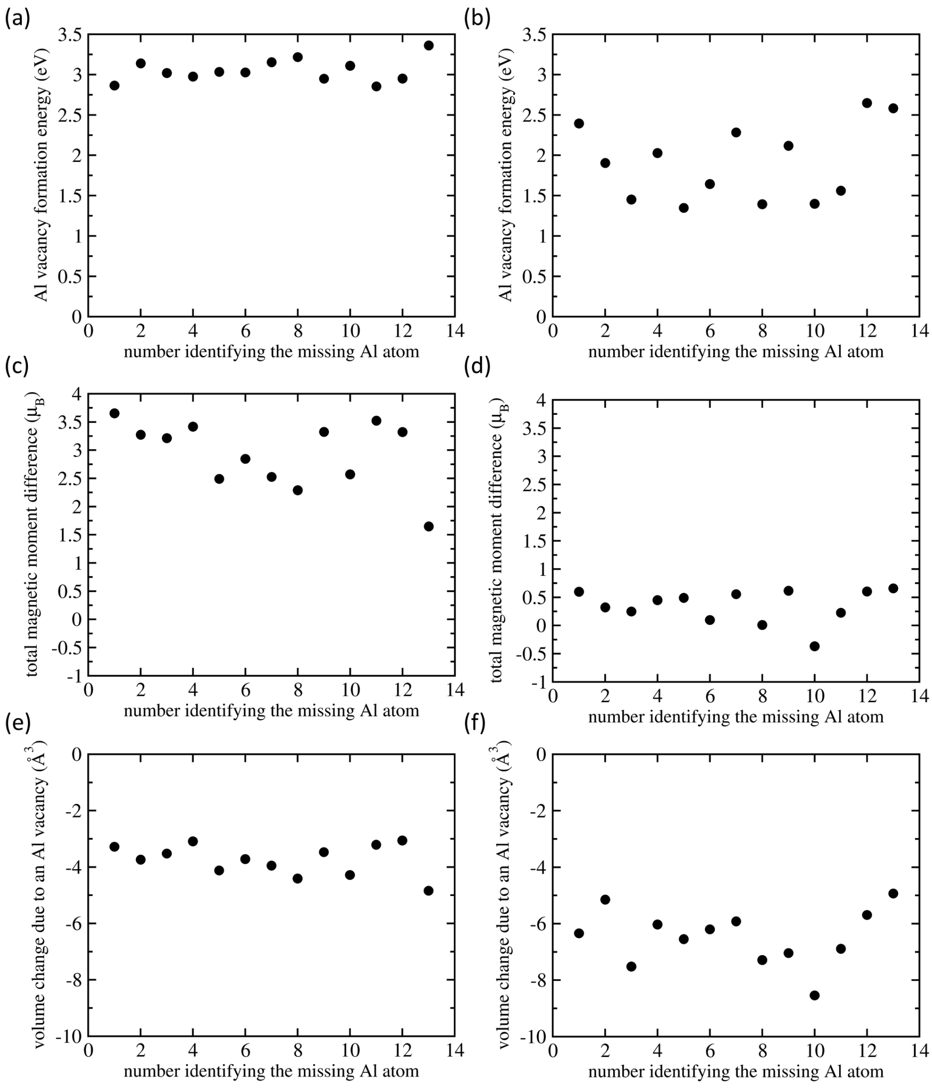

Figure 7. Computed formation energies of Al vacancies in the B2 (**a**) and A2 (**b**) phase together with the changes of the total magnetic moment of the whole supercell representing the B2 (**c**) and A2 (**d**) phase and the vacancy-induced volumetric changes for both the B2 (**e**) and A2 (**f**) phase.

The above-discussed mechanism is polymorph-sensitive. In contrast to the results for the B2 phase, where the Al atoms are limited to only one half of all possible atomic positions (i.e., one sublattice of the two in the B2 polymorph), the Al atoms are statistically distributed over all lattice sites in the A2 phase. Consequently, the above-mentioned increase of the total magnetic moment due to Al vacancies in the B2 polymorph is less pronounced in the A2 phase and the changes of the total magnetic moment are both positive and negative covering a significantly narrower range close to the zero value, see Figure 7d. The computed changes in magnetic moments can be possibly explained in terms of charge transfer that can be analyzed using, e.g., molecular orbital calculations [103]. Regarding the vacancy-induced volumetric changes, see Figure 7e,f, they are qualitatively similar to those in the case of Fe and Co vacancies.

4. Conclusions

We have performed a quantum-mechanical study of vacancy-induced changes in thermodynamic, structural and magnetic properties of single-phase ferromagnetic slightly non-stoichiometric Fe_2CoAl with a chemically disordered either two-sublattice B2 or single-sublattice A2 phase. The two polymorphs of Fe_2CoAl were modeled by two different 54-atom supercells with atoms on either two B2 sublattices or a single A2 sublattice distributed according to the special quasi-random structure (SQS) concept. Both the lower-energy B2 and higher-energy A2 phases were found to possess elastic constants that correspond to auxetic and mechanically stable systems. Our systematic removal of different atoms (one at a time) from the supercells resulted in quite wide ranges of values of vacancy-related characteristics. The increase in the level of disorder (when changing from the B2 phase to the A2 one) results in a further increase in the scatter of calculated values. In general, the Fe and Co vacancies have lower vacancy formation energies than the Al ones. The change from the B2 phase to the A2 phase typically means that the vacancy formation energies cover a wider range of values, in particular, including some quite low energies in the case of the A2 phase. The total magnetic moment of the whole supercell decreases when introducing Fe and Co vacancies but it increases in the B2 phase when an Al vacancy is introduced. The latter finding can be explained by an increase of the local magnetic moment of Fe atoms when the number of Al atoms in the first neighbor shell of Fe atoms is reduced, such as here due to an Al vacancy. In general, it often is easier to form the vacancies in the A2 structure than in the more stable B2 one. In the A2 structure, vacancies cause a more significant decrease (or a much lower increase in case of Al vacancy) in the total magnetic moment of the supercells and a higher decrease in their volume.

Author Contributions: Writing—Original Draft Preparation, visualization, M.F.; Conceptualization, Methodology, J.P., M.F. and M.Š.; Writing—Review & Editing, M.F., J.P. and M.Š.; Resources, Project Administration, Funding Acquisition, M.F.; Supervision: M.Š. All authors have read and agreed to the published version of the manuscript.

Funding: This research received no external funding.

Institutional Review Board Statement: Not applicable.

Informed Consent Statement: Not applicable.

Data Availability Statement: The data presented in this study are available on request from the corresponding author.

Acknowledgments: We gratefully acknowledge discussions with Yvonna Jirásková from the Institute of Physics of Materials, v.v.i., Czech Academy of Sciences, Brno, Czech Republic. Computational resources were provided by the Ministry of Education, Youth and Sports of the Czech Republic under the Projects e-INFRA CZ (ID:90140) at the IT4Innovations National Supercomputing Center and e-Infrastruktura CZ (e-INFRA LM2018140) at the MetaCentrum as well as the CERIT-Scientific Cloud (Project No. LM2015085), all granted within the program Projects of Large Research, Development and Innovations Infrastructures. M.F. and M.Š. acknowledge the support by the Czech Academy of Sciences (project No. UFM-A-RVO:68081723). The Figures 1 and 4 were visualized using the VESTA [104].

Conflicts of Interest: The authors declare no conflict of interest.

Appendix A

To evaluate the configurational entropy of the B2 and A2 phases, we use a generalized formula [105] derived for the sublattice model [106] $S^{\mathrm{conf}} = -R\sum_j a_j \sum_i f_i^j \ln f_i^j$ where R is the universal gas constant, i runs over different chemical species, j is the index of different sublattices, a_j is the number of lattice sites of a sublattice j divided by the total number of all lattice sites and f_i^j is the fraction of a chemical species i on a sublattice j. The configurational entropy is higher in the A2 phase than in the B2 phase by 0.03 meV/(K·atom). If the total energy difference of 86 meV per atom between the A2 and B2 phase should be compensated solely by the difference in the configurational entropy, it would happen at the temperature of 2880 K.

References

1. Heusler, F.; Starck, W.; Haupt, E. Über magnetische Manganlegierungen. *Verh. Dtsch. Phys. Ges.* **1903**, *5*, 219.
2. Gilleßen, M.; Dronskowski, R. A combinatorial study of full Heusler alloys by first-principles computational methods. *J. Comput. Chem.* **2009**, *30*, 1290. [CrossRef] [PubMed]
3. Gilleßen, M.; Dronskowski, R. A combinatorial study of inverse Heusler alloys by first-principles computational methods. *J. Comput. Chem.* **2010**, *31*, 612. [CrossRef]
4. Webster, P. Heusler Alloys. *Contemp. Phys.* **1969**, *10*, 559–577. [CrossRef]
5. Graf, T.; Felser, C.; Parkin, S.S.P. Simple rules for the understanding of Heusler compounds. *Prog. Solid State Chem.* **2011**, *39*, 1–50. [CrossRef]
6. Picozzi, S.; Continenza, A.; Freeman, A. Co_2MnX (X = Si, Ge, Sn) Heusler compounds: An ab initio study of their structural, electronic, and magnetic properties at zero and elevated pressure. *Phys. Rev. B* **2002**, *66*, 094421. [CrossRef]
7. Webster, P. Magnetic and chemical order in Heusler alloys containing cobalt and manganese. *J. Phys. Chem. Solids* **1971**, *32*, 1221. [CrossRef]
8. Kübler, J.; Williams, A.; Sommers, C. Formation and coupling of magnetic-moments in Heusler alloys. *Phys. Rev. B* **1983**, *28*, 1745–1755. [CrossRef]
9. Galanakis, I.; Dederichs, P.; Papanikolaou, N. Slater-Pauling behavior and origin of the half-metallicity of the full-Heusler alloys. *Phys. Rev. B* **2002**, *66*, 174429. [CrossRef]
10. Miura, Y.; Nagao, K.; Shirai, M. Atomic disorder effects on half-metallicity of the full-Heusler alloys $Co_2(Cr_{1-x}Fe_x)Al$: A first-principles study. *Phys. Rev. B* **2004**, *69*, 144413. [CrossRef]
11. Galanakis, I.; Dederichs, P.; Papanikolaou, N. Origin and properties of the gap in the half-ferromagnetic Heusler alloys. *Phys. Rev. B* **2002**, *66*, 134428. [CrossRef]
12. Kandpal, H.C.; Fecher, G.H.; Felser, C. Calculated electronic and magnetic properties of the half-metallic, transition metal based Heusler compounds. *J. Phys. D Appl. Phys.* **2007**, *40*, 1507–1523. [CrossRef]
13. Galanakis, I.; Mavropoulos, P.; Dederichs, P. Electronic structure and Slater-Pauling behaviour in half-metallic Heusler alloys calculated from first principles. *J. Phys. D Appl. Phys.* **2006**, *39*, 765–775. [CrossRef]
14. Buschow, K.; Van Engen, P. Magnetic and magneto-optical properties of Heusler alloys based on aluminum and gallium. *J. Magn. Magn. Mater.* **1981**, *25*, 90–96. [CrossRef]
15. Chadov, S.; Qi, X.; Kübler, J.; Fecher, G.H.; Felser, C.; Zhang, S.C. Tunable multifunctional topological insulators in ternary Heusler compounds. *Nat. Mater.* **2010**, *9*, 541–545. [CrossRef]
16. Lin, H.; Wray, L.A.; Xia, Y.; Xu, S.; Jia, S.; Cava, R.J.; Bansil, A.; Hasan, M.Z. Half-Heusler ternary compounds as new multifunctional experimental platforms for topological quantum phenomena. *Nat. Mater.* **2010**, *9*, 546–549. [CrossRef] [PubMed]
17. Planes, A.; Manosa, L.; Acet, M. Magnetocaloric effect and its relation to shape-memory properties in ferromagnetic Heusler alloys. *J. Phys. Condens. Matter* **2009**, *21*, 233201. [CrossRef]
18. Entel, P.; Buchelnikov, V.; Khovailo, V.; Zayak, A.; Adeagbo, W.; Gruner, M.; Herper, H.; Wassermann, E. Modelling the phase diagram of magnetic shape memory Heusler alloys. *J. Phys. D Appl. Phys.* **2006**, *39*, 865–889. [CrossRef]
19. Kainuma, R.; Imano, Y.; Ito, W.; Morito, H.; Sutou, Y.; Oikawa, K.; Fujita, A.; Ishida, K.; Okamoto, S.; Kitakami, O. Metamagnetic shape memory effect in a Heusler-type $Ni_{43}Co_7Mn_{39}Sn_{11}$ polycrystalline alloy. *Appl. Phys. Lett.* **2006**, *88*, 192513. [CrossRef]
20. Sauthoff, G. *Intermetallics*; VCH Verlagsgesellschaft: Weinheim, Germany, 1995.
21. Liu, C.T.; Stringer, J.; Mundy, J.N.; Horton, L.L.; Angelini, P. Ordered intermetallic alloys: An assessment. *Intermetallics* **1997**, *5*, 579–596. [CrossRef]
22. Stoloff, N.S. Iron aluminides: Present status and future prospects. *Mater. Sci. Eng. A* **1998**, *258*, 1–14. [CrossRef]

23. Liu, C.T.; Lee, E.H.; McKamey, C.G. An environmental-effect as the major cause for room-temperature embrittlement in FeAl. *Scr. Metall.* **1989**, *23*, 875–880. [CrossRef]
24. Lynch, R.J.; Heldt, L.A.; Milligan, W.W. Effects of alloy composition on environmental embrittlement of B2 ordered iron aluminides. *Scr. Metall.* **1991**, *25*, 2147–2151. [CrossRef]
25. Liu, C.T.; McKamey, C.G.; Lee, E.H. Environmental-effects on room-temperature ductility and fracture in Fe_3Al. *Scr. Metall.* **1990**, *24*, 385–389. [CrossRef]
26. Lynch, R.J.; Gee, K.A.; Heldt, L.A. Environmental embrittlement of single-crystal and thermomechanically processed B2-ordered iron aluminides. *Scr. Metall.* **1994**, *30*, 945–950. [CrossRef]
27. Zamanzade, M.; Barnoush, A.; Motz, C. A review on the properties of iron aluminide intermetallics. *Crystals* **2016**, *6*, 10. [CrossRef]
28. Kattner, U.; Burton, B. Al-Fe (Aluminium-Iron). In *Phase Diagrams of Binary Iron Alloys*; Okamoto, H., Ed.; ASM International: Materials Park, OH, USA, 1993; pp. 12–28.
29. Palm, M.; Inden, G.; Thomas, N. The Fe-Al-Ti system. *J. Phase Equilibria* **1995**, *16*, 209–222. [CrossRef]
30. Vernieres, J.; Benelmekki, M.; Kim, J.H.; Grammatikopoulos, P.; Bobo, J.F.; Diaz, R.E.; Sowwan, M. Single-step gas phase synthesis of stable iron aluminide nanoparticles with soft magnetic properties. *APL Mater.* **2014**, *2*, 116105. [CrossRef]
31. Jirásková, Y.; Pizúrová, N.; Titov, A.; Janičkovič, D.; Friák, M. Phase separation in Fe-Ti-Al alloy—Structural, magnetic, and Mössbauer study. *J. Magn. Magn. Mater.* **2018**, *468*, 91–99. [CrossRef]
32. Palm, M.; Lacaze, J. Assessment of the Al-Fe-Ti system. *Intermetallics* **2006**, *14*, 1291–1303. [CrossRef]
33. Dobeš, F.; Dymáček, P.; Friák, M. Force-to-stress conversion methods in small punch testing exemplified by creep results of Fe-Al alloy with chromium and cerium additions. *IOP Conf. Ser. Mater. Sci. Eng.* **2018**, *461*, 012017. [CrossRef]
34. Dobeš, F.; Dymáček, P.; Friák, M. Small punch creep of Fe-Al-Cr alloy with Ce addition and its relation to uniaxial creep tests. *Kov. Mater. Met. Mater.* **2018**, *56*, 205. [CrossRef]
35. Palm, M.; Sauthoff, G. Deformation behaviour and oxidation resistance of single-phase and two-phase $L2_1$-ordered Fe-Al-Ti alloys. *Intermetallics* **2004**, *12*, 1345–1359. [CrossRef]
36. Sundman, B.; Ohnuma, I.; Dupin, N.; Kattner, U.R.; Fries, S.G. An assessment of the entire Al-Fe system including D0(3) ordering. *Acta Mater.* **2009**, *57*, 2896–2908. [CrossRef]
37. Dymáček, P.; Dobeš, F.; Jirásková, Y.; Pizúrová, N.; Friák, M. Tensile, creep and fracture testing of prospective Fe-Al-based alloys using miniature specimens. *Theor. Appl. Fract. Mech.* **2019**, *99*, 18–26. [CrossRef]
38. Dobeš, F.; Dymáček, P.; Friák, M. The influence of niobium additions on creep resistance of Fe-27 at. % Al alloys. *Metals* **2019**, *9*, 739. [CrossRef]
39. Luo, X.; Cao, J.; Meng, G.; Zhou, Y.; Xie, H. Long-range-ordered Fe_3Al with excellent electromagnetic wave absorption. *J. Mater. Sci.-Mater. Electron.* **2020**, *31*, 15608–15615. [CrossRef]
40. Ismail, A.; Bahanan, W.; Bin Hussain, P.; Saat, A.M.; Shaik, N.B. Diffusion bonding of Al-Fe enhanced by gallium. *Processes* **2020**, *8*, 824. [CrossRef]
41. Grigorchik, A.N.; Astrashab, V, E.; Kukareko, V.A.; Belotserkovsky, M.A.; Sosnovsky, V.A. High-temperature heat treatment of hypersonic metallization coatings from pseudoalloy “Fe-Al”. *Lett. Mater.* **2021**, *11*, 198–203. [CrossRef]
42. Deevi, S.C. Advanced intermetallic iron aluminide coatings for high temperature applications. *Prog. Mater. Sci.* **2021**, *118*. [CrossRef]
43. Tolochyn, O.I.; Baglyuk, G.A.; Tolochyna, O.V.; Evych, Y.I.; Podrezov, Y.M.; Molchanovska, H.M. Structure and physicomechanical properties of the Fe_3Al intermetallic compound obtained by impact hot compaction. *Mater. Sci.* **2021**, *56*, 499–508. [CrossRef]
44. Komarov, O.N.; Zhilin, S.G.; Predein, V.V.; Popov, A.V. Mechanisms for forming iron-containing intermetallics prepared by aluminothermy and the effect of special treatment methods on their properties. *Metallurgist* **2020**, *64*, 810–821. [CrossRef]
45. Vodičková, V.; Švec, M.; Hanus, P.; Novák, P.; Záděra, A.; Keller, V.; Prokopčáková, P.P. The effect of simultaneous Si and Ti/Mo alloying on high-temperature strength of Fe_3Al-based iron aluminides. *Molecules* **2020**, *25*, 4268. [CrossRef]
46. Luo, X.; Cao, J.; Meng, G.; Chuan, Y.; Yao, Z.; Xie, H. Systematical investigation on the microstructures and tribological properties of Fe-Al laser cladding coatings. *Appl. Surf. Sci.* **2020**, *516*, 146121. [CrossRef]
47. Luo, X.; Cao, J.; Meng, G.; Yu, F.; Jiang, Q.; Zhang, P.; Xie, H. Double glow plasma surface metallurgy technology fabricated Fe-Al-Cr coatings with excellent corrosion resistance. *Coatings* **2020**, *10*, 575. [CrossRef]
48. Teker, T.; Yilmaz, S.O. Synthesis and structural characterization of Fe based Ti+Ni_3Al+Al_2O_3 reinforcement composite produced by mechanical alloying. *Rev. Metal.* **2020**, *56*, 4. [CrossRef]
49. Zhang, X.; Sun, Y.; Niu, M.; Shao, M.; Geng, X. Microstructure and mechanical behavior of in situ TiC reinforced Fe_3Al (Fe-23Al-3Cr) matrix composites by mechanical alloying and vacuum hot-pressing sintering technology. *Vacuum* **2020**, *180*, 109544. [CrossRef]
50. Ghazanfari, H.; Blais, C.; Gariepy, M.; Savoie, S.; Schulz, R.; Alamdari, H. Improving wear resistance of metal matrix composites using reinforcing particles in two length-scales: Fe_3Al/TiC composites. *Surf. Coatigs Technol.* **2020**, *386*, 125502. [CrossRef]
51. Khodaei, M. Characterization of Al_2O_3 in Fe_3Al-30 vol.% Al_2O_3 nanocomposite powder synthesized by mechanochemical process. *J. Nanostruct.* **2020**, *10*, 456–462. [CrossRef]
52. Altunin, R.R.; Moiseenko, E.T.; Zharkov, S.M. Structural phase transformations during a solid-state reaction in a bilayer Al/Fe thin-film nanosystem. *Phys. Solid State* **2020**, *62*, 200–205. [CrossRef]

53. Tolochyn, O.I.; Tolochyna, O.V.; Bagliuk, H.A.; Yevych, Y.I.; Podrezov, Y.M.; Mamonova, A.A. Influence of sintering temperature on the structure and properties of powder iron aluminide Fe_3Al. *Powder Metall. Met. Ceram.* **2020**, *59*, 150–159. [CrossRef]
54. Adler, L.; Fu, Z.; Koerner, C. Electron beam based additive manufacturing of Fe_3Al based iron aluminides—Processing window, microstructure and properties. *Mater. Sci. Eng. A* **2020**, *785*, 139369. [CrossRef]
55. Michalcová, A.; Ozkan, M.; Mikula, P.; Marek, I.; Knaislová, A.; Kopeček, J.; Vojtěch, D. The influence of powder milling on properties of SPS compacted FeAl. *Molecules* **2020**, *25*, 2263. [CrossRef] [PubMed]
56. Peska, M.; Karczewski, K.; Rzeszotarska, M.; Polanski, M. Direct synthesis of Fe-Al alloys from elemental powders ssing laser engineered net shaping. *Materials* **2020**, *13*, 531. [CrossRef] [PubMed]
57. Watson, R.E.; Weinert, M. Transition-metal aluminide formation: Ti, V, Fe, and Ni aluminides. *Phys. Rev. B* **1998**, *58*, 5981–5988. [CrossRef]
58. Gonzales-Ormeno, P.; Petrilli, H.; Schön, C. Ab-initio calculations of the formation energies of BCC-based superlattices in the Fe-Al system. *Calphad-Comput. Coupling Ph. Diagrams Thermochem.* **2002**, *26*, 573. [CrossRef]
59. Connetable, D.; Maugis, P. First principle calculations of the kappa-Fe_3AlC perovskite and iron-aluminium intermetallics. *Intermetallics* **2008**, *16*, 345–352. [CrossRef]
60. Kellou, A.; Grosdidier, T.; Raulot, J.M.; Aourag, H. Atomistic study of magnetism effect on structural stability in Fe_3Al and Fe_3AlX (X = H, B, C, N, O) alloys. *Phys. Status Solidi B-Basic Solid State Phys.* **2008**, *245*, 750–755. [CrossRef]
61. Šesták, P.; Friák, M.; Holec, D.; Všianská, M.; Šob, M. Strength and brittleness of interfaces in Fe-Al superalloy nanocomposites under multiaxial loading: An ab initio and atomistic study. *Nanomaterials* **2018**, *8*, 873. [CrossRef] [PubMed]
62. Lechermann, F.; Fähnle, M.; Meyer, B.; Elsässer, C. Electronic correlations, magnetism, and structure of Fe-Al subsystems: An LDA+U study. *Phys. Rev. B* **2004**, *69*, 165116. [CrossRef]
63. Airiskallio, E.; Nurmi, E.; Heinonen, M.H.; Vayrynen, I.J.; Kokko, K.; Ropo, M.; Punkkinen, M.P.J.; Pitkanen, H.; Alatalo, M.; Kollar, J.; et al. High temperature oxidation of Fe-Al and Fe-Cr-Al alloys: The role of Cr as a chemically active element. *Corros. Sci.* **2010**, *52*, 3394–3404. [CrossRef]
64. Lechermann, F.; Welsch, F.; Elsässer, C.; Ederer, C.; Fähnle, M.; Sanchez, J.; Meyer, B. Density-functional study of Fe_3Al: LSDA versus GGA. *Phys. Rev. B* **2002**, *65*, 132104. [CrossRef]
65. Friák, M.; Slávik, A.; Miháliková, I.; Holec, D.; Všianská, M.; Šob, M.; Palm, M.; Neugebauer, J. Origin of the low magnetic moment in Fe_2AlTi: An Ab initio study. *Materials* **2018**, *11*, 1732. [CrossRef] [PubMed]
66. Friák, M.; Oweisová, S.; Pavlů, Jana Holec, D.; Šob, M. An ab initio study of thermodynamic and mechanical stability of Heusler-based Fe_2AlCo polymorphs. *Materials* **2018**, *11*, 1543. [CrossRef] [PubMed]
67. Ju, J.; Kang, M.; Zhou, Y.; Yang, C.; Wang, K.; Li, J.; Wang, R.; Fu, H.; Wang, J. First-principles investigations of the stability, electronic structures, mechanical properties and thermodynamic properties of $Fe_xAl_yC_z$ compounds in Fe-Cr-B-Al-C alloy. *J. Phys. Chem. Solids* **2020**, *143*, 109366. [CrossRef]
68. Miháliková, I.; Friák, M.; Jirásková, Y.; Holec, D.; Koutná, N.; Šob, M. Impact of nano-scale distribution of atoms on electronic and magnetic properties of phases in Fe-Al nanocomposites: An ab initio study. *Nanomaterials* **2018**, *8*, 1059. [CrossRef] [PubMed]
69. Friák, M.; Holec, D.; Šob, M. Quantum-mechanical study of nanocomposites with low and ultra-low interface energies. *Nanomaterials* **2018**, *8*, 1057. [CrossRef] [PubMed]
70. Kulikov, N.I.; Postnikov, A.V.; Borstel, G.; Braun, J. Onset of magnetism in B2 transition-metal aluminides. *Phys. Rev. B* **1999**, *59*, 6824–6833. [CrossRef]
71. Friák, M.; Neugebauer, J. Ab initio study of the anomalous volume-composition dependence in Fe-Al alloys. *Intermetallics* **2010**, *18*, 1316–1321. [CrossRef]
72. Ipser, H.; Semenova, O.; Krachler, R. Intermetallic phases with $D0_3$-structure: A statistical-thermodynamic model. *J. Alloys Compd.* **2002**, *338*, 20–25. [CrossRef]
73. Fähnle, M.; Drautz, R.; Lechermann, F.; Singer, R.; Diaz-Ortiz, A.; Dosch, H. Thermodynamic properties from ab-initio calculations: New theoretical developments, and applications to various materials systems. *Phys. Status Solidi B-Basic Solid State Phys.* **2005**, *242*, 1159–1173. [CrossRef]
74. Kirklin, S.; Saal, J.E.; Hegde, V.I.; Wolverton, C. High-throughput computational search for strengthening precipitates in alloys. *Acta Mater.* **2016**, *102*, 125–135. [CrossRef]
75. Liu, S.; Duan, S.; Ma, B. First-principles calculation of vibrational entropy for Fe-Al compounds. *Phys. Rev. B* **1998**, *58*, 9705–9709.
76. Čížek, J.; Lukáč, F.; Procházka, I.; Kužel, R.; Jirásková, Y.; Janičkovič, D.; Anwand, W.; Brauer, G. Characterization of quenched-in vacancies in Fe-Al alloys. *Phys. B* **2012**, *407*, 2659–2664. [CrossRef]
77. Miháliková, I.; Friák, M.; Koutná, N.; Holec, D.; Šob, M. An ab initio study of vacancies in disordered magnetic systems: A case study of Fe-rich Fe-Al phases. *Materials* **2019**, *12*, 1430. [CrossRef] [PubMed]
78. Amara, H.; Fu, C.C.; Soisson, F.; Maugis, P. Aluminum and vacancies in α-iron: Dissolution, diffusion, and clustering. *Phys. Rev. B* **2010**, *81*, 174101. [CrossRef]
79. Friák, M.; Černý, M.; Všianská, M.; Šob, M. Impact of antiphase boundaries on structural, magnetic and vibrational properties of Fe_3Al. *Materials* **2020**, *13*, 4884. [CrossRef]
80. Li, Y.; Liu, Y.; Yang, J. First principle calculations and mechanical properties of the intermetallic compounds in a laser welded steel/aluminum joint. *Opt. Laser Technol.* **2020**, *122*, 105875. [CrossRef]

81. Friák, M.; Černý, M.; Šob, M. The effect of hydrogen on the stress-strain response in Fe_3Al: An ab initio molecular-dynamics study. *Materials* **2021**, *14*, 4155. [CrossRef]
82. Grover, A.K.; Pillay, R.G.; Nagarajan, V.; Tandon, P.N. Site preference and local environment effects in ferromagnetic ternary alloys. *J. Magn. Magn. Mater.* **1980**, *15*, 699–700. [CrossRef]
83. Zunger, A.; Wei, S.; Ferreira, L.; Bernard, J. Special quasirandom structures. *Phys. Rev. Lett.* **1990**, *65*, 353–356. [CrossRef]
84. Oganov, A.R.; Glass, C.W. Crystal structure prediction using ab initio evolutionary techniques: Principles and applications. *J. Chem. Phys.* **2006**, *124*, 244704. [CrossRef] [PubMed]
85. Lyakhov, A.O.; Oganov, A.R.; Stokes, H.T.; Zhu, Q. New developments in evolutionary structure prediction algorithm USPEX. *Comput. Phys. Commun.* **2013**, *184*, 1172–1182. [CrossRef]
86. Oganov, A.R.; Lyakhov, A.O.; Valle, M. How evolutionary crystal structure prediction works—And why. *Accounts Chem. Res.* **2011**, *44*, 227–237. [CrossRef]
87. Zhou, L.; Holec, D.; Mayrhofer, P.H. First-principles study of elastic properties of Cr-Al-N. *J. Appl. Phys.* **2013**, *113*, 043511. [CrossRef]
88. Moakher, M.; Norris, A.N. The closest elastic tensor of arbitrary symmetry to an elasticity tensor of lower symmetry. *J. Elast.* **2006**, *85*, 215–263. [CrossRef]
89. Kresse, G.; Hafner, J. Ab initio molecular dynamics for liquid metals. *Phys. Rev. B* **1993**, *47*, 558–561. [CrossRef]
90. Kresse, G.; Furthmüller, J. Efficient iterative schemes for ab initio total-energy calculations using a plane-wave basis set. *Phys. Rev. B* **1996**, *54*, 11169–11186. [CrossRef] [PubMed]
91. Hohenberg, P.; Kohn, W. Inhomogeneous electron gas. *Phys. Rev. B* **1964**, *136*, B864–B871. [CrossRef]
92. Kohn, W.; Sham, L.J. Self-consistent equations including exchange and correlation effects. *Phys. Rev. A* **1965**, *140*, A1133–A1138. [CrossRef]
93. Blöchl, P.E. Projector augmented-wave method. *Phys. Rev. B* **1994**, *50*, 17953–17979. [CrossRef] [PubMed]
94. Kresse, G.; Joubert, D. From ultrasoft pseudopotentials to the projector augmented-wave method. *Phys. Rev. B* **1999**, *59*, 1758–1775. [CrossRef]
95. Perdew, J.P.; Wang, Y. Accurate and simple analytic representation of the electron-gas correlation energy. *Phys. Rev. B* **1992**, *45*, 13244–13249. [CrossRef]
96. Vosko, S.H.; Wilk, L.; Nusair, M. Accurate spin-dependent electron liquid correlation energies for local spin density calculations: A critical analysis. *Can. J. Phys.* **1980**, *58*, 1200. [CrossRef]
97. Monkhorst, H.J.; Pack, J.D. Special points for Brillouin-zone integrations. *Phys. Rev. B* **1976**, *13*, 5188–5192. [CrossRef]
98. Friák, M.; Gracias, J.; Pavlů, J.; Šob, M. A quantum-mechanical study of antiphase boundaries in ferromagnetic B2-phase Fe_2CoAl alloy. *Magnetochemistry* **2021**, *7*, 137. [CrossRef]
99. Mouhat, F.; Coudert, F.M.C.X. Necessary and sufficient elastic stability conditions in various crystal systems. *Phys. Rev. B* **2014**, *90*, 224104. [CrossRef]
100. Friák, M.; Lago, D.; Koutná, N.; Holec, D.; Rebok, T.; Šob, M. Multi-phase ELAStic Aggregates (MELASA) software tool for modeling anisotropic elastic properties of lamellar composites. *Comput. Phys. Commun.* **2019**, *247*, 106863. [CrossRef]
101. Gaillac, R.; Pullumbi, P.; Coudert, F.X. ELATE: An open-source online application for analysis and visualization of elastic tensors. *J. Phys. Condens. Matter* **2016**, *28*, 275201. [CrossRef] [PubMed]
102. Friák, M.; Buršíková, V.; Pizúrová, N.; Pavlů, J.; Jirásková, Y.; Homola, V.; Miháliková, I.; Slávik, A.; Holec, D.; Všianská, M.; et al. Elasticity of phases in Fe-Al-Ti superalloys: Impact of atomic order and anti-phase boundaries. *Crystals* **2019**, *9*, 299. [CrossRef]
103. Glaus, S.; Calzaferri, G.; Hoffmann, R. Electronic properties of the silver–silver chloride cluster interface. *Chem. Eur. J.* **2002**, *8*, 1785–1794. [CrossRef]
104. Momma, K.; Izumi, F. VESTA 3 for three-dimensional visualization of crystal, volumetric and morphology data. *J. Appl. Crystallogr.* **2011**, *44*, 1272–1276. [CrossRef]
105. Miracle, D.; Senkov, O. A critical review of high entropy alloys and related concepts. *Acta Mater.* **2017**, *122*, 448–511. [CrossRef]
106. Hillert, M. *Phase Equilibria, Phase Diagrams and Phase Transformations: Their Thermodynamic Basis*, 2nd ed.; Cambridge University Press: Cambridge, UK, 2008.